Available online at www.sciencedirect.com
SCIENCE DIRECT®
PERGAMON
International Journal of Multiphase Flow 29 (2003) 1523–1549
International Journal of Multiphase Flow
www.elsevier.com/locate/ijmulflow

The effects of a highly viscous liquid phase on vertically upward two-phase flow in a pipe

David A. McNeil *, Alastair D. Stuart

School of Engineering and Physical Sciences, Department of Mechanical and Chemical Engineering, Heriot–Watt University, Naysmith building, Edinburgh EH14 4AS, UK

Received 14 November 2002; received in revised form 10 June 2003

Abstract

Water and glycerine solutions were used to produce nominal liquid viscosities of 1, 50, 200 and 550 mPa s. These liquids flowed concurrently with air to allow measurements of momentum flux, void fraction and pressure distributions to be made at mass fluxes consistent with an exit "homogeneous" Mach number of 0.4. The flow pattern in the pipe was, in the main, annular up-flow. The data are shown to be consistent with the annular flow model. However, entrained liquid fractions were estimated at conditions where they were unexpected and the interfacial friction factors were significantly different to those implied from low viscosity fluid correlations. A new correlation for the interfacial friction factor is proposed for the highly viscous dataset. Choking tests were carried out with air–liquid flows with liquid viscosities of 1 and 50 mPa s. These data showed that the annular model approach extends to cover these flow conditions. More traditional methods are shown not to represent the measured void fraction, frictional pressure drop or choking mass flow rates.

Keywords: Two-phase flow; Annular flow; Vertical upward flow; Liquid viscosity; Pressure drop; Liquid film thickness; Interfacial friction factor

1. Introduction

If a runaway reaction occurs during the manufacture of some products, such as styrene, some of the fluid needs to be blown down to protect the reactor from excessive pressure. In such a situation, the chemical reaction may continue within the fluid during its passage through the

* Corresponding author. Tel.: +44-131-449-5111; fax: +44-131-451-3129.
E-mail address: d.a.mcneil@hw.ac.uk (D.A. McNeil).

0301-9322/$ - see front matter
doi:10.1016/S0301-9322(03)00122-8

venting system. The solid content dissolving within the liquid will cause the liquid viscosity to increase, giving rise to a highly viscous two-phase flow. Current design knowledge is restricted in this area, causing some uncertainty in how blow down systems will perform in these circumstances. This study was undertaken to improve the basis on which these designs are made.

Highly viscous single-phase flow of Newtonian fluids in pipes is probably one of the most understood areas of fluid mechanics. However, its two-phase counterpart is an area that has received little attention, although some studies have been done. Furukawa and Fukano (2001) used glycerine solutions with viscosities of up to 15 mPa s to investigate the effects of liquid viscosity on flow pattern. Fukano and Furukawa (1998) used glycerine solutions with viscosities of up to 10 mPa s to investigate the effect of liquid viscosity on interfacial shear stress and frictional pressure drop. Mori and Nakano (2001) used glycerine solutions with viscosities of up to 70 mPa s to investigate the inception of roll waves and droplets, while Kondo et al. (1999) used viscosities of up to 20 mPa s to investigate the effect of liquid viscosity on interfacial waves. All of these studies have shown that increasing the liquid viscosity had a significant effect on the phenomena studied. However, the level of viscosity used by these investigators was considerably lower than the values envisaged here, where viscosities of 50,000 mPa s are possible. Studies at this level of viscosity have been recently undertaken for other geometries, e.g. Campanile and Azzopardi (2001). This study was initiated to test the applicability of current knowledge when the viscosity of the liquid phase is significantly increased in a vertically upward pipe flow, and to improve that knowledge where it is found to be deficient.

2. Experimental

The pressure gradient in a two-phase flow has three components, gravitational, accelerational and frictional. Experiments were undertaken using four different fluids in a purpose built test facility to investigate the effect of liquid viscosity on these by monitoring the void fraction, momentum flux and pressure gradient.

2.1. Test fluids

The characteristics of the fluids were obtained prior to their use in the experimental programme. For tests involving water, the viscosity was taken as 1 mPa s and the density as 1000 kg/m^3. Three viscous fluids were obtained by combining glycerine with water at various concentrations. The viscosities of these solutions were obtained by analysing samples in a Carri-Med viscometer controlled by a PC. The measurements indicated that the shear stress was proportional to the strain rate and that the constant of proportionality was strongly dependent on temperature, i.e. the fluids were Newtonian. The viscosity of each fluid was characterised by correlating this constant with a cubic polynomial in temperature. The densities of the test solutions were established by measuring the weight of a known volume of liquid. The glycerine–water solutions had nominal viscosities of 550, 200 and 50 mPa s. The corresponding densities were 1260, 1235 and 1190 kg/m^3. The viscosity ranges present within the dataset were 560–740, 220–260 and 42–54 mPa s. The viscosity of glycerine varies significantly with water concentration, particularly at low levels. Viscosity measurements were repeated frequently throughout the test programme. The

variation in surface tension between the water value of 0.072 N/m and the glycerine value of 0.063 N/m was not measured in this study. Where this was required by an established correlation, the pure glycerine value was used for all glycerine–water mixtures.

2.2. Test facility

A schematic of the test facility is shown in Fig. 1. The facility could be operated using single-phase liquid, single-phase air or two-phase air–liquid flows. The facility had three flow loops that

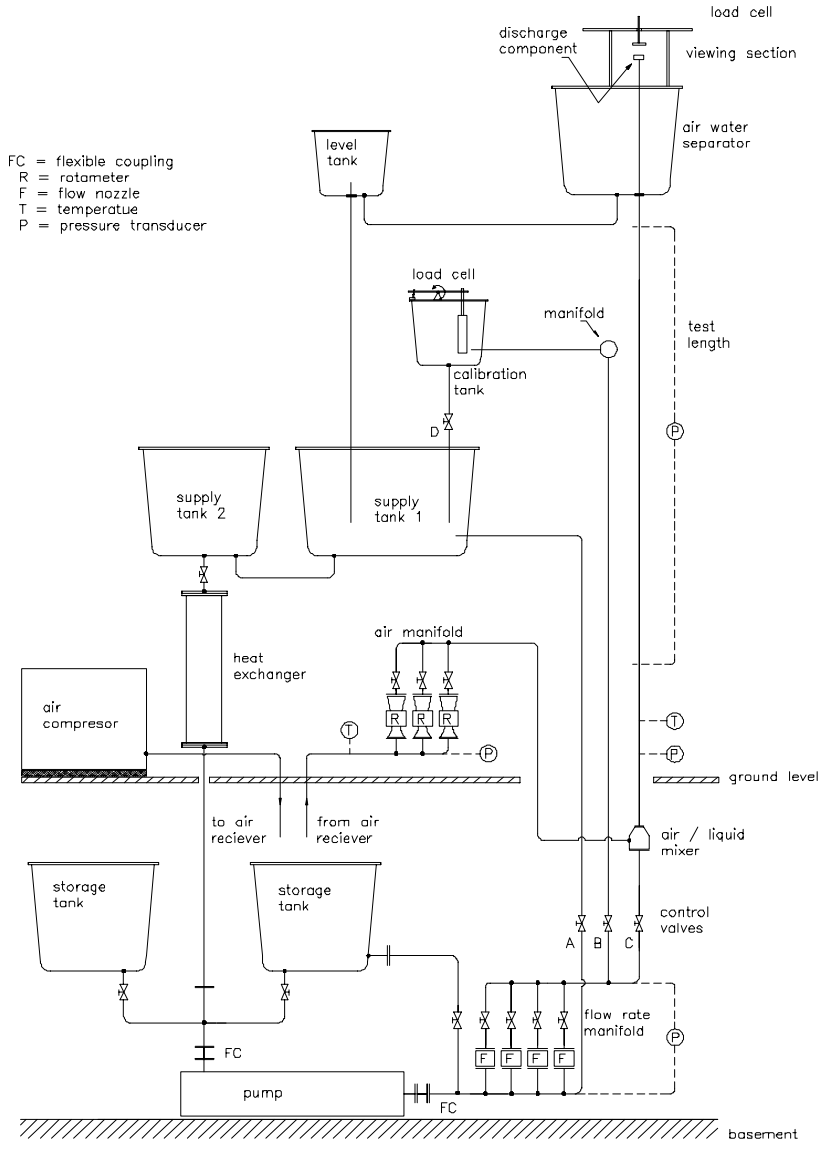

Fig. 1. Test facility layout.

the liquid could pass around, the re-circulating loop, the flowmeter calibration loop and the test loop. Only one loop existed for air.

The re-circulation loop had liquid from the supply tanks pass through the heat exchanger, the pump, control valve A and back to the supply tanks. The interconnection between the supply tanks and the piping between the heat exchanger and the pump were constructed from PVC piping components 100 mm in diameter. This piping was necessary to prevent the frictional pressure drop exceeding the gravitational pressure rise and thus inducing cavitation in the pump. The remaining pipe work on this loop was constructed from copper pipeline components, 50 mm in diameter. This flow loop was always used when liquid was flowing and was necessary to balance the liquid flow through either the calibration or test loops with the flow through the progressive cavity pump. The heat exchanger was used to control the liquid temperature by removing the internal heating resulting from pipe friction. It was cooled using tap water.

The calibration and test loops both used the bank of four parallel flow nozzles (Fig. 1). The pipe work upstream of the nozzles was constructed from copper components 50 mm in diameter. The remainder was constructed from copper components 26 mm in diameter. Only one of these loops was in operation at any one time.

The flow calibration loop was used to calibrate the flow measurement nozzles for use in the test loop. With valve B open and valves C and D closed, Fig. 1, liquid was taken from the supply tanks and delivered to the pump. The pump pushed the liquid through two loops, the re-circulation and the flow calibration loops. The liquid in the calibration loop passed from the pump, through the flow nozzle being calibrated, through valve B and into the calibrated collection tanks. The flow rate through the flow nozzle was controlled by adjusting valve A. A thermocouple placed downstream of valve B allowed the liquid temperature to be measured and thus the liquid viscosity to be estimated. A Rosemount 3051 differential pressure transmitter was used to measure the flow nozzle pressure drop. The volume flow rate through the flow nozzle was established from a timed collection in the calibrated tanks. After the timed collection had been made, liquid was returned to the supply tank by opening valve D. For viscous liquids the discharge coefficient depends on the throat Reynolds number (Alvi et al., 1978). The discharge coefficient was linked to the throat Reynolds number through a cubic equation.

The test loop was operated with valve B closed and valve C open (Fig. 1). Liquid was again delivered to the pump from the supply tanks and pumped through two circuits, the re-circulation loop and the test loop. The liquid in the test loop passed through the flow nozzle to valve C. A thermocouple was placed downstream of valve C to allow the test temperature to be measured and thus the liquid viscosity to be estimated. From valve C the liquid moved through the air–liquid mixer and into the test section. Liquid from the test section was delivered to the discharge section. Just upstream of the discharge flange was a pressure tap connected to a Rosemount 2088 gauge pressure transmitter. This allowed the pressure at the discharge to be measured so that choked flow could be detected. Liquid from the discharge section passed into a glass observation chamber that was vented to the atmosphere. The discharging liquid impinged on a flat plate target set at 90° to the flow. The target was 100 mm in diameter and was placed 90 mm above the liquid discharge point. The force on the target was measured using two load cells mounted in parallel. This allowed the momentum flow rate of the discharging liquid to be determined. Liquid flowed from the target to the air–liquid separator, where it drained, via the separator level control tank, onto a series of four plates angled at 30° to the horizontal and onto the supply tanks. The angled

plates provided a surface area of 6 m^2 and were used to aid the removal of small bubbles entrained in the liquid phase.

The air stream flowed from an air receiver that was charged to a pressure of 7.5 bar by a dedicated compressor. Filtered air from the receiver was passed to one of the three magnetically coupled rotameters with ranges, 0–0.0037, 0–0.033 and 0–0.325 kg/s. The pressure and temperature of the air entering the rotameters were measured on a Bourdon gauge and a thermocouple respectively. Air from the rotameters passed through the air–liquid mixer and into the test section, before discharging onto the load cell target. It thereafter entered the air–liquid separator and was discharged to the atmosphere.

Two-phase operation was achieved by operating the liquid test loop and the air loop simultaneously. The liquid flow was established prior to the airflow being set. The air and liquid flows were brought together via an annulus section 15 mm long, with the air occupying the inner pipe, 22 mm in diameter, and the liquid occupying the space between the outside of the air pipe and the test pipe. A two-phase flow therefore existed from the air–liquid mixer to the air–liquid separator. Additionally, when viscous liquids were used, a fan took the air from the separator exit and passed it through a PVC pipe 100 mm in diameter to a discharge point outside of the building. This proved a necessary additional step because very fine liquid droplets were entrained in the discharging air stream. Prior to this additional step, these produced a smog-like cloud above the discharge point of the separator that set off the fire alarms. This did not occur with air–water tests.

The high viscosity two-phase tests were particularly difficult to complete. The discharging two-phase mixture entrained very small gas bubbles in the glycerine–water solutions. Thus, over a period of time, the liquid in the supply tanks became laden with air bubbles. After about 30 min the bubbles could be viewed near the base of the glass heat exchanger. Testing ceased when this was observed, giving this as the maximum time to set the required conditions and obtain all the readings for a particular test. The heat exchanger is connected to the pump by 2.2 m of vertical pipe, 100 mm in diameter. Air–laden liquid was therefore never unintentionally injected. The small gas bubbles took about 10 h to disengage from the liquid. Thus, only one experimental point could be obtained in a working day. Immersion heaters were added to the supply tanks so that the fluid viscosity could be reduced between tests, thus allowing the air bubbles to disengage more quickly. This allowed two test points to be obtained in a working day.

2.3. Test section

The test section is shown in Fig. 2. The test section comprised of a settling length 2.8 m long, an upstream pressure gradient measurement section that contained five pressure tappings 250 mm apart, a spool piece 200 mm long and a downstream pressure gradient measurement section that contained five pressure tappings 500 mm apart. The settling length had a length to diameter ratio of 107, sufficient to give a reasonably well-developed flow within the test section. The pressure tappings, Fig. 2, were connected to a purging/measuring system by ball valves. The system was constructed from stainless steel tube 10 mm in diameter and was coupled to a Rosemount 2088 gauge pressure transmitter and to both the air and liquid supplies, allowing purging with either. Each pressure tapping was purged and read in sequence. A gamma-ray densitometer was located between the last two pressure tappings of the downstream pressure gradient measurement section. This was used to determine the void fraction during the two-phase tests.

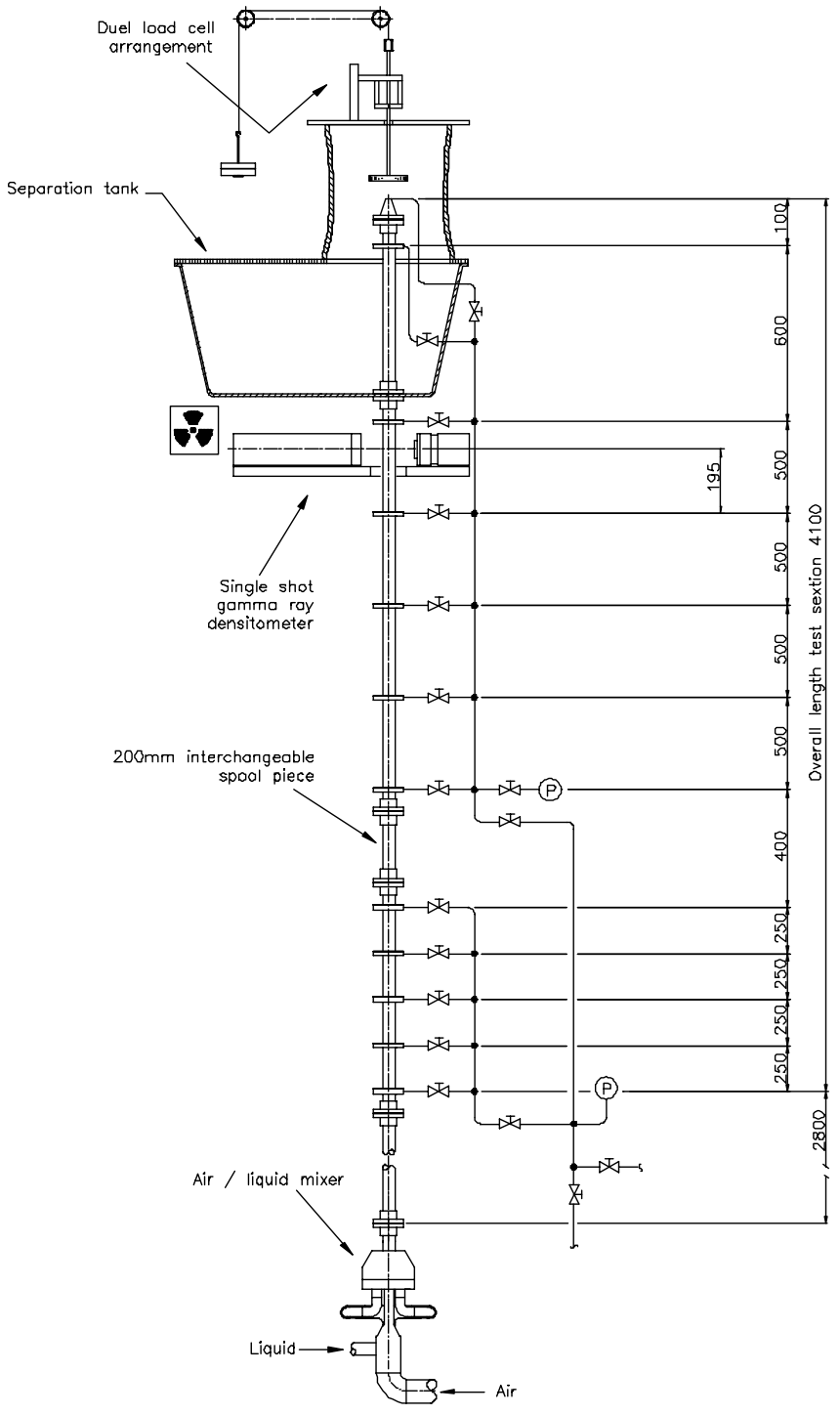

Fig. 2. Test section.

2.4. Miscellaneous

The gamma-ray densitometer, the load cells and the pressure transmitters were read by a PC based, data acquisition system. The temperatures, the Bourdon gauge and the air rotameter readings were entered into the PC manually. A hundred pressure readings and 50 load cell readings were collected and averaged for each measurement. These numbers were chosen after a study of the signals produced from a range of conditions showed them to be sufficient to determine the averages. The liquid flow nozzles were accurate to ±1% and the air rotameters to ±1.6% of reading. The pressure transmitters were of the SMART type. The operating span was set prior to a test by a HART communicator. The pressure transmitters were accurate to ±0.2% of reading. The thermocouples were K-type and were connected to a Comark microprocessor thermometer. This gave a discrimination of ±0.1 °C. The load cells were calibrated over their range of 0–4 kg by placing known weights upon them. This was repeatable to ±0.2% of reading. The diameter of the test section was found by filling it with water and draining and weighing the contents. The pipe was found to have a diameter of 26.12 mm.

For a single-phase laminar flow in a pipe, the theoretical friction factor, f_L, is related to the Reynolds number, Re_L, through

$$f_L = \frac{16}{Re_L} \tag{1}$$

When the viscosity measurements and the flow nozzle calibrations were used together with the pressure-gradient measurements, corrected for gravitational effects, agreement with the theoretical friction factors were obtained to better than ±5%.

2.5. Test conditions

Two types of test were carried out, subsonic and sonic. The mass flow rates for the subsonic tests were chosen to give exit Mach numbers of about 0.4 at nominal qualities of 0.04, 0.06, 0.08, 0.1, 0.2, 0.4, 0.6 and 0.8. The Mach number was based on the homogeneous flow model and the quality was taken as the ratio of the gas mass flow rate to the total mass flow rate. This gave mass fluxes ranging from 900 kg/m^2 s at the lowest quality to 180 kg/m^2 s at the highest quality. Additionally with the 550 mPa s fluid, these qualities were repeated at mass fluxes ranging from 920 to 240 kg/m^2 s, taking the test facility to its design limits. Sonic tests were carried out using water and the 50 mPa s fluid. The mass flow rates for the sonic tests were arrived at by increasing the liquid and gas flows incrementally until an exit pressure above atmospheric was achieved. The same nominal qualities as those previously listed were used, giving a mass flux range of 2200–500 kg/m^2 s.

3. Flow pattern

Direct flow pattern observations were not made. However, the lower bound of the quality range that was employed was selected because it was the approximate point where significant vibrations of the load cells did not occur during the air–water tests. The experimental conditions at the test

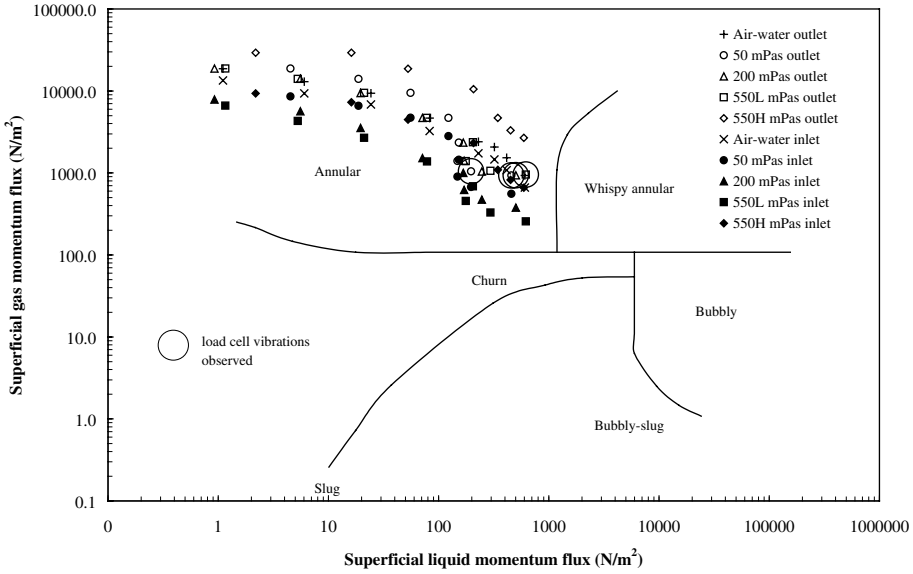

Fig. 3. Vertical flow map of Hewit and Roberts (1969).

section inlet and the pipe discharge are shown on the vertical flow map of Hewit and Roberts (1969) in Fig. 3. The air–water data are shown to be in the annular flow regime, as are all of the other data points. Shifts in the location of the data points away from the annular-churn boundary are shown to occur between the test section inlet and the discharge point for all data, with the 550 mPa s data displaced the most. This occurred because the very large pressure drops that occurred with the high viscosity fluids gave rise to substantial velocity and density variations within the test section. The highly viscous data points where the load cells vibrated significantly are circled in Fig. 3. These data indicate that this flow map does not give accurate boundaries for highly viscous fluids. Furukawa and Fukano (2001) have shown that viscosity has an effect on the flow map boundaries and that the froth annular transition defined on the horizontal flow map of Baker (1954) can be reasonably applied to vertical flows. The experimental conditions at the test section inlet and the pipe discharge are shown on the Baker flow map in Fig. 4. The highly viscous data points where the load cells vibrated significantly are again circled. The air–water and 50 mPa s data are shown to be in the annular flow regime with the lower quality data for the 200 and 550 mPa s data shown to be in the froth regime. Furukawa and Fukano (2001) used fluids with a viscosity up to 15 mPa s. This is considerably lower than was used here. The indications are that their observations do not extrapolate to these viscosities. However, it is also clear that most data were taken in the annular flow regime although some may have been taken in the churn flow regime.

4. Data reduction method for subsonic flows

In analysing the data several assumptions were made. Firstly, it was assumed that the fluid flow could be described by an annular flow model, where the liquid close to the wall travelled in a

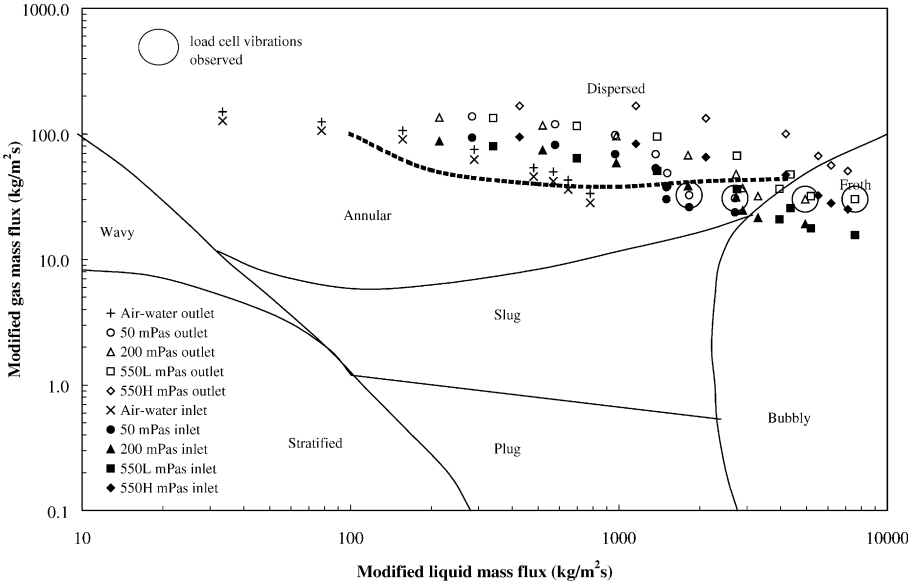

Fig. 4. Horizontal flow map of Baker (1954).

liquid film of thickness δ at a lower velocity than the gas moving in the centre of the tube. A fraction of the liquid, ε, could be entrained in the gas to form the core flow. This liquid was assumed to travel at the gas velocity. This assumption was investigated by obtaining terminal velocity estimates for the drops. The estimates were based on the actual mass flow rates and pressure gradients, the drop size correlation reported by Ambrosini et al. (1991) and the drag coefficients used by Richter (1983). These indicated that the droplet to gas velocity ratios were greater than 0.9 for the viscous fluids. The annular flow assumption was also not considered limiting, because, as reported by Holt et al. (1999), the annular flow model works well in the annular and churn flow regimes, the regimes that the data were obtained in, Section 3. Secondly, it was assumed that acceleration effects could be neglected in the liquid film flow. This allowed a momentum equation to be written for that flow as

$$\frac{\mathrm{d}p}{\mathrm{d}z} = \frac{(\tau_\mathrm{i} - \tau_\mathrm{w})}{\delta} - \frac{g}{v_\mathrm{L}} \tag{2}$$

where p is the pressure, z is the distance from the test section inlet, g is the acceleration due to gravity, v_L is the liquid specific volume and τ_i and τ_w are the shear stresses at the core-liquid film interface and wall respectively. The corresponding momentum equation for the core flow is

$$\frac{\mathrm{d}p}{\mathrm{d}z} = -\frac{4\tau_\mathrm{i}}{(D-2\delta)} - \frac{g}{v_\mathrm{c}} - \dot{m}_\mathrm{c}^2 \frac{\mathrm{d}v_\mathrm{c}}{\mathrm{d}z} \tag{3}$$

where D is the pipe diameter, v_c is the specific volume of the core flow, given by

$$v_\mathrm{c} = \frac{(x v_\mathrm{G} + \varepsilon(1-x)v_\mathrm{L})}{(x + \varepsilon(1-x))} \tag{4}$$

and $\dot{m}_c$ is the core mass flux, given by

$$\dot{m}_c = \frac{4\left(\dot{M}_G + \varepsilon \dot{M}_L\right)}{\pi(D-2\delta)^2} \tag{5}$$

with v_G being the gas specific volume; x, the quality of the flow and $\dot{M}_G$ and $\dot{M}_L$, the mass flow rates of gas and liquid respectively. Thirdly, it was assumed that the gas flowed isothermally and could be treated as perfect, thus

$$\frac{dp}{dv_G} = -\frac{p}{v_G} \tag{6}$$

Finally, it was assumed that the thickness of the liquid film could be evaluated using the method of Ambrosini et al. (1991). This method related a non-dimensional film thickness, δ_L^+, to the film Reynolds number, Re_{LF}, thus

$$\delta_L^+ = B Re_{LF}^n = \frac{\delta}{\mu_L}\sqrt{\frac{\tau_c}{v_L}} \tag{7}$$

where μ_L is the liquid viscosity and τ_c is a characteristic shear stress given by

$$\tau_c = \frac{(\tau_i + 2\tau_w)}{3} \tag{8}$$

The liquid film Reynolds number is given by

$$Re_{LF} = \frac{(1-\varepsilon)(1-x)\dot{m}D}{\mu_L} \tag{9}$$

where $\dot{m}$ is the total mass flow rate per unit pipe area. When the film Reynolds number is less than 1000, the flow is laminar and the coefficient B and the index n are 0.34 and 0.6 respectively. When the film Reynolds number is greater than 1000, the flow is turbulent and the coefficient B and the index n are 0.0512 and 0.875 respectively.

A 'best-fit' quadratic equation was obtained from the 10 pressure readings and was differentiated to determine the pressure gradient at any required location. The entrained liquid fraction was specified, as described in Section 6, to allow the core specific volume gradient to be determined from

$$\frac{dv_c}{dz} = \frac{dv_c}{dp}\frac{dp}{dz} = \frac{x}{(x+\varepsilon(1-x))}\frac{dv_G}{dp}\frac{dp}{dz} \tag{10}$$

allowing the film thickness, and the interfacial and wall shear stresses to be determined by the simultaneous solution of Eqs. (2)–(10). The flow property ranges obtained from the subsonic dataset are listed in Table 1. Dataset 550L refers to the 550 mPa s data obtained at the same mass fluxes used for the other viscosities, while 550H refers to those obtained at the higher mass fluxes (Section 2.5).

Table 1
Deduced flow property ranges

Fluid viscosity (mPa s)	Pressure drop (bar)	Gas velocity (m/s)	Liquid film velocity (m/s)	Interfacial shear stress (N/m^2)	Wall shear stress (N/m^2)
1	0.32–0.37	22–120	1.9–4.2	48–67	48–68
50	0.45–0.92	22–100	0.21–2.1	58–176	57–180
200	1.0–1.5	17–96	0.47–2.0	140–310	160–350
550L	1.4–2.2	12–87	0.5–2.1	220–400	250–520
550H	1.6–2.7	17–110	0.37–2.0	210–500	220–610

5. Jet force measurements

Traditionally, a jet force, F, has been expressed as the product of the force that would occur if the flow were all liquid and a two-phase multiplier, ϕ_{LO}^2 (see e.g. Chisholm, 1983). Thus,

$$F = \phi_{LO}^2 \frac{\pi}{4} D^2 \dot{m}^2 v_L \tag{11}$$

Forces were not obtained at all of the experimental conditions, mainly because of load cell vibrations. The momentum two-phase multipliers obtained are shown against quality for each fluid in Fig. 5. Also included in the figure are the lines corresponding to the values that would be obtained if the flow were homogeneous or exhibiting "maximum slip" behaviour. Maximum slip is said to occur when the entrained liquid fraction is zero and the slip ratio, the ratio of average gas to the average liquid velocity, is given by the square root of the ratio of the gas to liquid specific volumes. As expected, the air–water data follow the homogeneous flow line at qualities

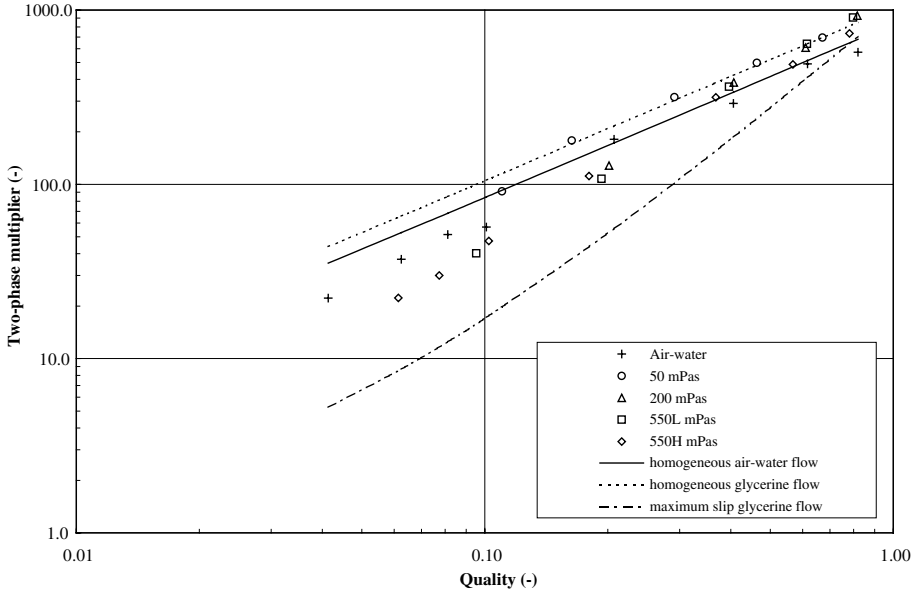

Fig. 5. Comparison of momentum two-phase mulipliers.

above 0.1 and fall away from this line at qualities below this. The 50 mPa s data behave similarly; however, the higher viscosity data are substantially below the homogeneous line for all but the highest quality. This would suggest that the higher viscosity fluids have a lower entrained liquid fraction than the lower viscosity fluids.

For the assumptions made in Section 4, the force exerted by the jet discharging from the test facility onto the target can be determined from

$$F = \dot{M}((x + \varepsilon(1-x))u_G + (1-\varepsilon)(1-x)u_{LF}) = c_m \frac{\pi}{4} D^2 \dot{m}^2 v \tag{12}$$

where u_G and u_{LF} are the gas and liquid film velocities respectively, v is the specific volume of the two-phase mixture, given by

$$v = \frac{(xv_G + k(1-x)v_L)}{(x + k(1-x))} \tag{13}$$

and c_m is the momentum correction factor that corrects for the assumed velocity distribution of the phases and is given by

$$c_m = (x + k(1-x))\left(x + (1-x)\left(\varepsilon + \frac{(1-\varepsilon)^2}{(k-\varepsilon)}\right)\right) \tag{14}$$

(see e.g. McNeil, 1998). The assumption that the entrained liquid travels at the gas velocity allows the area occupied by the entrained liquid, and hence the core area, to be found. A re-arrangement of this relationship allows the slip ratio to be found from

$$k = \frac{\varepsilon}{\alpha_c} + \frac{(1-\alpha_c)}{\alpha_c}\frac{x}{(1-x)}\frac{v_G}{v_L} \tag{15}$$

where α_c is the core area fraction given by

$$\alpha_c = \left(1 - \frac{2\delta}{D}\right)^2 \tag{16}$$

These equations allow the entrained liquid fraction to be estimated as follows. The pressure gradient at the pipe exit was obtained by extrapolating the test-section, pressure-gradient equation to the pipe exit. This gradient, atmospheric pressure and a guess to the entrained liquid fraction were imposed on Eqs. (2)–(10) to allow the conditions at the pipe exit to be estimated. The momentum flow rate exiting the pipe, Eqs. (12)–(16), was compared with the force registered on the load cells. The entrained liquid fraction was systematically altered and the process repeated until a balance was achieved. This model of the flow neglects some physical phenomena that may be present, such as huge or disturbance waves. Any increases in momentum flux arising from these phenomena will register as an increase in the entrained liquid fraction. In essence, these measurements indicate the extent to which the liquid phase requires two characteristic velocities. At zero entrained liquid only the film value is required, whereas at all entrained only the gas value is needed. In between both are required. The maximum force that this model of the flow can generate is the homogeneous value, a value reached when the entrained liquid fraction tends to unity. The measured force was above the homogeneous value once with water, four times with the

50 mPa s liquid, once with the 200 mPa s liquid, once during the 550L mPa s tests and never during the 550H mPa s tests. The corresponding under-predictions were 5%, 3–8%, 10% and 8%.

Fig. 6 shows a comparison between the variations in estimated entrained liquid fractions with superficial gas velocity for each fluid. Predictions of the air–water entrained liquid fraction using the methods of Govan et al. (1988) and Pan and Hanratty (2002) are included in Fig. 6. The prediction method proposed by Govan et al. (1988) was evaluated by assuming a fully developed flow. This occurs when there is a balance between the rates of entrained and deposited liquid droplets. The discharge point where the jet forces were measured was 268 pipe diameters downstream of the two-phase mixer, which, according to Chong et al. (2001) was enough to justify this assumption. Both of these methods require a critical Reynolds number, below which all of the liquid flows in the liquid film, i.e. the entrained liquid fraction is zero. In a recent study by Chong et al. (2001), using a large body of fluids, the critical Reynolds number associated with the Govan et al. (1988) method was found to best represent the available data. This critical Reynolds number was used with both methods. The air–water data are shown to follow the trend of both methods reasonably well.

For the same superficial gas velocity, the 50 mPa s data are shown to lie above the air–water data, with the higher viscosity fluids shown to lie below them. Thus, increasing the viscosity seems to increase the level of entrained liquid in the core flow until some maximum is reached, and decrease it thereafter. A turning characteristic is evident in the air–water flow that is not present in the 50, 200 and 550L mPa s data, but is present in the 550H mPa s data. Turning characteristics are associated with a critical Reynolds number. The model of Pan and Hanratty (2002) can be fitted to the 550H mPa s dataset, as shown in Fig. 6, by setting the critical gas velocity to zero, their A_1 coefficient to 5.88×10^{-6} and the critical Reynolds number to 2.5. Their A_1 constant was

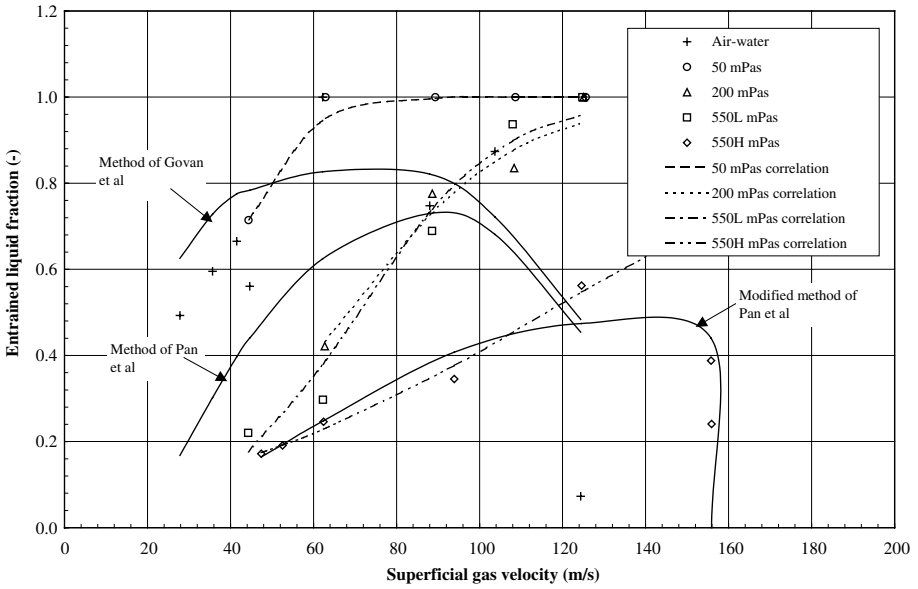

Fig. 6. Variation of entrained liquid fraction with superficial gas velocity.

an order of magnitude larger than this and their critical Reynolds number was two orders of magnitude larger. The behaviour is mimicked but the mechanisms are unlikely to be the same. The 550L and 550H datasets show a considerably different variation of entrained liquid fraction with superficial gas velocity, despite having the same nominal liquid viscosity. At the lower gas velocity of about 45 m/s, the 550L and 550H datasets have superficial liquid velocities of 0.4 and 0.7 m/s respectively and the entrained liquid fractions are about the same at 0.2. However, when the superficial gas velocity is increased to 125 m/s, the 550L and 550H datasets have superficial liquid velocities of 0.03 and 0.2 m/s respectively, an order of magnitude different, and leading to entrained liquid fractions of 0.99 and 0.56 respectively. The entrained liquid fraction depends on the liquid velocity.

The critical Reynolds number method used gave a value of 430 for water and approximately 350 for the other fluids. Without entrained liquid, the film Reynolds number ranges were 870–20,300 for water, 35–420 for the 50 mPa s fluid, 3–80 for the 200 mPa s fluid and 1–40 for the 550 mPa s fluid. This critical Reynolds number criterion therefore suggests that entrained liquid should only exist at one of the viscous fluid test conditions. Fig. 6 clearly shows that entrained liquid fractions are being established well below the point that it occurs in low viscosity fluids, where the onset of entrained liquid is associated with the appearance of roll waves on the liquid films. Ishii and Grolmes (1975) reported an onset of entrained liquid model for viscous fluids that was not associated with roll waves. This model predicts a critical Reynolds number of less than one, allowing entrained liquid to exist at all of the test conditions. However, its inclusion in the Govan et al. (1988) model leads to entrained liquid fractions greater than 0.85, while its inclusion in the Pan and Hanratty (2002) model leads to entrained liquid fractions greater than 0.65, significantly greater than many of those estimated.

Pan and Hanratty (2002) avoided high viscosity fluids in developing their correlation for entrained liquid. They did so because other studies had shown that the diameter of the entrained liquid was much smaller than the low viscosity counterparts, and therefore much less likely to redeposit. This is consistent with the pipe discharges described in Section 2.2, where a baffle separator was sufficient to remove the entrained water drops from the air stream but not the glycerine drops that gave rise to the smog-like clouds produced at the separator discharge.

From these estimates and observations of entrained liquid fraction, viscous liquids behave differently from low viscosity liquids. The measurement method cannot differentiate between actual entrained liquid and liquid travelling near the gas velocities in a wave crest. Mori and Nakano (2001) found that for viscous fluids, roll waves appeared at Reynolds numbers above 200 and that the entrained liquid fraction increased slowly to this point and increased more swiftly thereafter. This critical Reynolds number is considerably higher than that of the vast majority of the viscous data obtained in this study, and their observations are based on fluids with a much lower liquid viscosity. However, it may be the case that the entrained liquid fraction may simply increase slowly with gas superficial velocity, as observed, since no rapid increase mechanism is available. This is not consistent with the 550H mPa s dataset, Fig. 6, a dataset obtained at higher liquid and gas flow rates. Different mechanisms may therefore exist at different conditions. Alternatively, wave behaviour may account for the increase in momentum flux or it may result from both causes. This does not matter to this study, since analysis of the data only requires the two-phase momentum flux to be estimated, irrespective of the source of the high-speed liquid. At a

deeper level, there is a gap in the understanding of entrained liquid, a gap that will require a detailed study of these phenomena.

6. Void fraction measurements

For a two-phase flow, the void fraction can be determined from

$$\alpha = \frac{x v_G}{(x v_G + k(1-x) v_L)} \tag{17}$$

The gamma-ray densitometer was located between the last two pressure tappings in the test section (Fig. 2). The pressure and pressure gradient at the densitometer were obtained from the best-fit pressure equation. The data reduction methodology outlined in Section 4 was used to estimate the local conditions at the densitometer once the entrained liquid fraction had been specified. These conditions allowed the slip ratio to be determined from Eqs. (15) and (16), allowing the void fraction to be found from Eq. (17). For air–water flows the method of Govan et al. (1988) was used for the entrained liquid fraction. For the viscous fluids it was estimated at the pipe discharge, as described in Section 5. It was necessary to "extrapolate" these results to conditions within the test section. Mori and Nakano (2001) suggested that the onset of entrained liquid did not have a critical liquid velocity in viscous fluids. The Govan et al. (1988) method was therefore used with the critical Reynolds number set to zero to simulate entrained liquid fraction distributions for the test mass flux range. The work of Pan and Hanratty (2002) suggested that the ratio $\varepsilon/(1-\varepsilon)$ can be used as a correlating parameter if the critical Reynolds number is zero. The discharge values from the simulations were used to obtain the square root of this parameter, which was correlated by a quadratic equation in superficial gas velocity. This correlation was found to predict the simulated in-tube entrained liquid fractions to within ±10%. This method was adapted for the viscous fluids on the assumption that similar processes will exist in high viscosity flows, an assumption that may not be valid (Section 5). The extrapolations are for each fluid and are based on actual momentum flux measurements at the discharge point. Any major discrepancy resulting from this assumption would get progressively worse as the distance to the discharge point increased. This was not observed. The discharge entrained liquid fractions were correlated for each liquid by an equation of the form

$$\sqrt{\frac{\varepsilon}{1-\varepsilon}} = H \exp(G u_{Gs}) \tag{18}$$

where G and H are the constants listed in Table 2.

Table 2
Entrained liquid fraction correlation coefficients

Viscosity (mPa s)	G (–)	H (–)
50	0.0546	0.141
200	0.0245	0.188
550L	0.0292	0.127
550H	0.0113	0.269

The 50 mPa s data constants were obtained by setting the first homogeneous value to 0.95. The 550H mPa s values were obtained by omitting the values obtained at the highest two gas velocities, consistent with setting the critical Reynolds number to zero (Section 5). The rest were obtained by "best-fits" to the datasets. A comparison between the correlations and the data are included in Fig. 6. The predictions of entrained liquid were included in the data reduction methodology to allow the void fraction to be determined. These void fractions are compared to the measured values in Fig. 7. The film method outlined is based on the work of Ambrosini et al. (1991). However, at these Reynolds numbers, only the element due to Asali et al. (1985) is being tested and is shown to predict the void fraction reasonably well. The work of Asali et al. (1985) only included fluids with viscosities of up to 5 mPa s, giving Film Reynolds numbers from 20 to 250. The fact that is works so well despite this is probably due to the mechanistic approach of the method. Included in Fig. 7 is the correlation of Premoli et al. (1970). This correlation was developed for low viscosity fluids and agrees well with the air–water results. However, it significantly over-predicts the highly viscous data. The separated flow model allows the void fraction to be determined from the frictional two-phase multiplier, see e.g. Collier and Thome (1994), thus

$$\alpha = 1 - \frac{1}{\sqrt{\phi_{\mathrm{L}}^2}} \tag{19}$$

This two-phase multiplier method is also compared to the measured data in Fig. 7. The multiplier was found from Eq. (21) with the C coefficient set to 25 (Section 7.1). The multiplier approach adequately predicts the air–water data but significantly under-predicts the data from the viscous fluids.

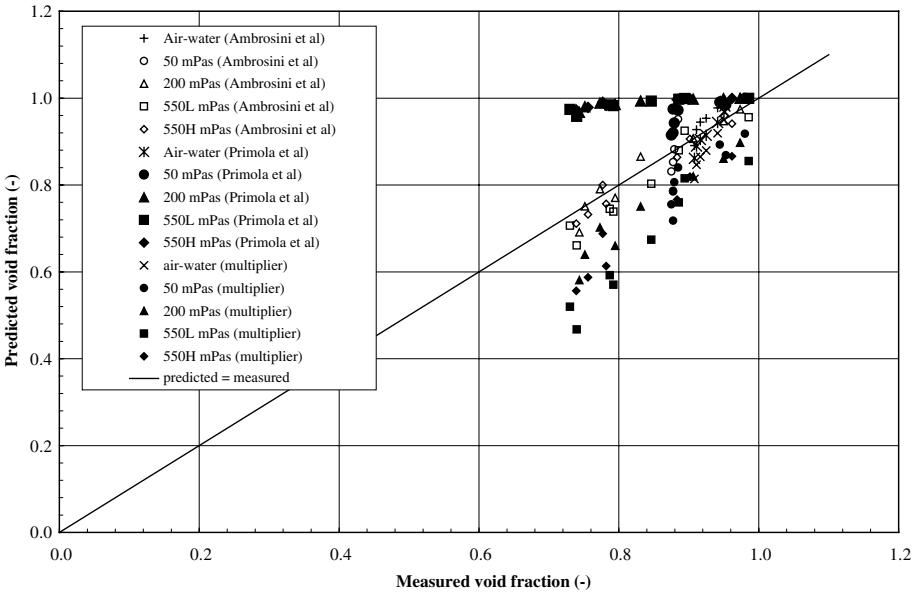

Fig. 7. Variation of predicted and measured void fraction.

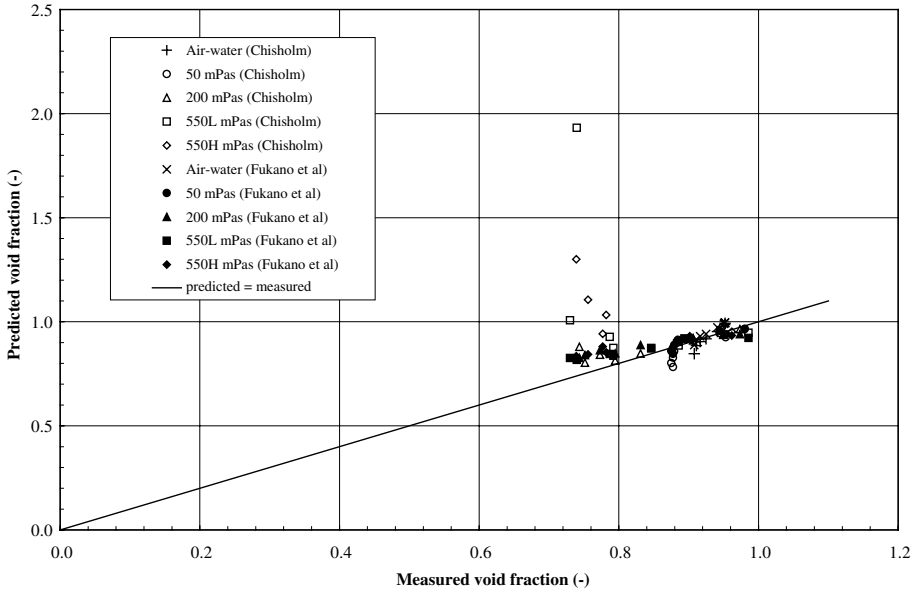

Fig. 8. Variation of predicted and measured void fraction.

Chisholm (1962) produced a correlation for the slip ratio of viscous fluids. The viscosity range of the liquids used was 1–267 mPa s. The film method of Fukano and Furukawa (1998) and the correlation of Chisholm (1962) are compared to the measured data in Fig. 8. The Chisholm (1962) correlation works well within the bounds of the data used in its formulation but fails for the highest viscosity fluid when the correlation becomes non-physical. The Fukano and Furukawa (1998) method agrees well with the lower viscosity data but diverges as the viscosity increases, in line with being formulated from data with liquid viscosities of up to 10 mPa s.

Of the methods tested, only the film model outlined in Section 4 predicts the measured void fraction trends, adding support to the analysis method outlined in Section 4.

7. Pressure drop measurements

Pressure drops have three components, accelerational, which depends and momentum flux as investigated in Section 5, gravitational, which depends on void fraction investigated in Section 6, and frictional. The pressure drop measurements were therefore used to investigate the frictional component. There are several ways to model frictional pressure drops, the most common being the two-phase multiplier and the interfacial friction factor approaches.

7.1. Two-phase multipliers

Two-phase multiplier methods can be used in a variety of ways. One popular way is to express the two-phase wall shear stress as the product of the value that would occur if only the liquid fraction flowed in the pipe and a two-phase multiplier, ϕ_L^2. Thus,

$$\tau_w = \frac{f_L}{2}(1-x)^2 \dot{m}^2 v_L \phi_L^2 \tag{20}$$

where the friction factor is based on the liquid only flow and is given by the Blasius equation for turbulent flow and by Eq. (1) for laminar flow. The data reduction methodology described in Section 4 was used to determine the wall shear stress, which was put into Eq. (20) to determine the experimental two-phase multiplier. The method of Govan et al. (1988) was used for the air–water entrained liquid fraction with the relationships deduced in Section 6 used for the other fluids. The use of the entrained liquid fraction relationships does not have a significant effect on the measured wall shear stresses for the viscous fluids because the frictional pressure gradient is a very large fraction of the overall pressure drop. The ranges of wall shear stresses observed are listed in Table 1. As expected, increasing the viscosity increases the wall shear stress.

The method of Chisholm (1983), referred to as the Chisholm C method, is based on this liquid-only approach and gives the multiplier as

$$\phi_L^2 = 1 + \frac{C}{X} + \frac{1}{X^2} \tag{21}$$

where X is the Martinelli parameter, given by

$$X = \frac{(1-x)}{x}\left(\frac{f_L}{f_G}\frac{v_L}{v_G}\right)^{0.5} \tag{22}$$

and the gas friction factor was evaluated similarly to the liquid value, except that only the gas component was assumed to flow in the pipe. Suggested values of the C coefficient are 21 if the gas and liquid flows are turbulent and 10 if the gas is turbulent and the liquid is laminar. The experimental data are compared with these suggestions in Fig. 9. The air–water data are in the turbulent–turbulent regime and should therefore correlate with $C = 21$. This is reasonably true. All of the other data are in the laminar liquid–turbulent gas regime and should correlate with $C = 10$. This is not true. In fact a single value of $C = 25$ correlates all of the data. The increase in C for the air–water data is not that significant. In fact, Chisholm and Laird (1958) obtained 26 for air–water flows in a 27 mm vertical pipe. However, for the other fluids the result is significant. For the 50 mPa s data, $0.2 < X < 2.6$, for the 200 mPa s data, $0.3 < X < 6.9$ and for the 550 mPa s data, $0.5 < X < 15$. Thus, the $1/X^2$ term is relatively small in comparison to the $1/X$ term, making the multiplier strongly dependent on C. Thus the typical coefficients suggested, mostly derived from low liquid flow rates of low viscosity liquids, do not extrapolate to high viscosity fluids.

Another method used to describe the two-phase wall shear stress, similar in concept to that just described, is to relate it to the liquid value based on all of the fluid being liquid. This removes the $(1-x)$ term from Eq. (20) and causes the friction factors to be evaluated assuming all of the fluid is either liquid or gas. Friedel (1979) deduced a predictive method of this type. Fig. 10 shows a comparison between the method and the experimental data. Again the air–water data are reasonably well predicted. However, as the viscosity increases, a progressive over-prediction occurs. This method was again derived from a data bank dominated by low viscosity fluids and clearly does not extrapolate to higher viscosity fluids.

The advice commonly offered on two-phase multiplier methods, see e.g. Collier and Thome (1994), is that if the ratio of the liquid to gas viscosity is less than 1000 Friedel (1979) should be

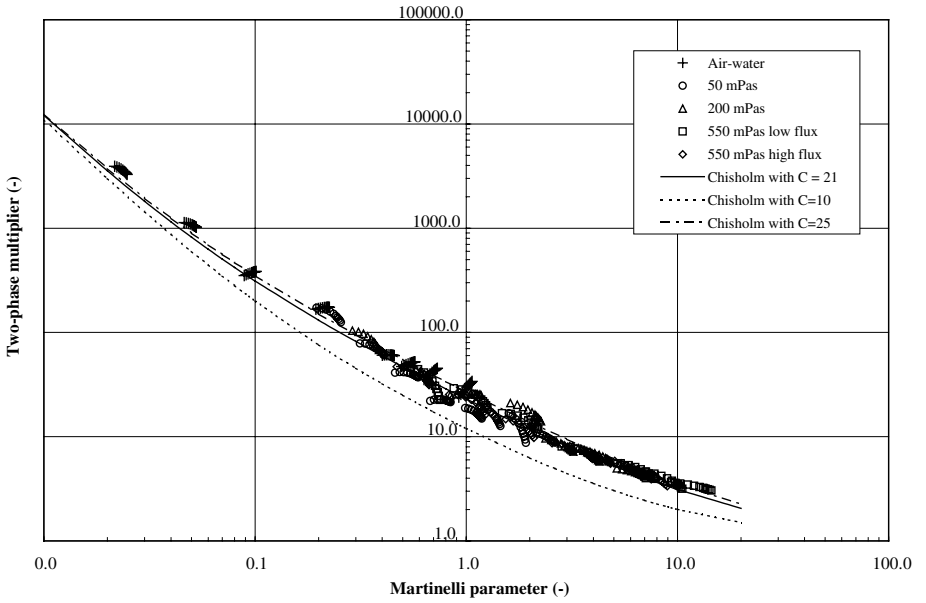

Fig. 9. Comparison of predicted and measured two-phase multiplier.

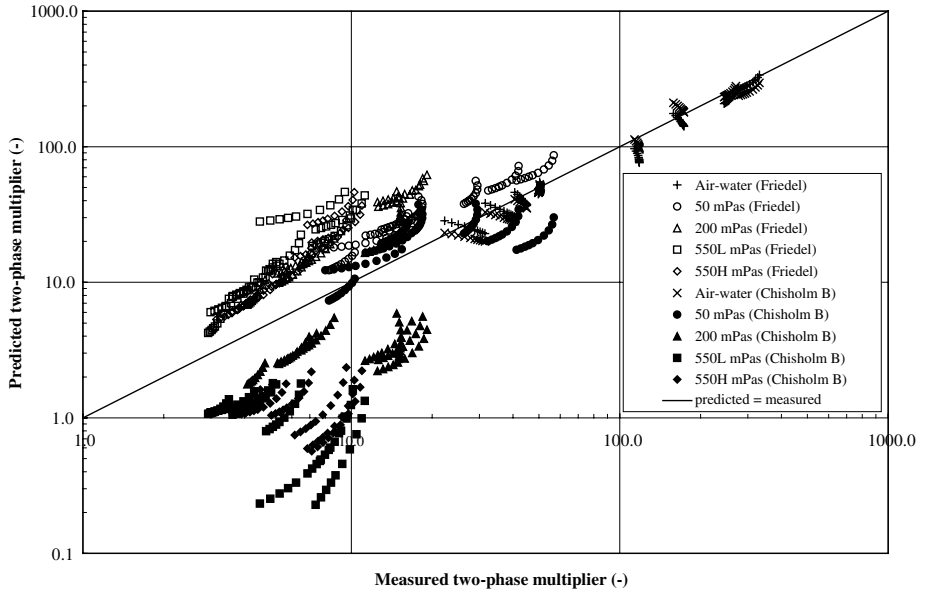

Fig. 10. Comparison of predicted and measured two-phase multiplier.

used. However, if the ratio of the liquid to gas viscosity is greater than 1000 and the mass flux is greater than 100 kg/m^2 s, Chisholm (1973), referred to as the Chisholm B method, should be used, with Chisholm C used otherwise. Thus, the Chisholm B method is recommended for the viscous

data obtained in this study. The Chisholm B method is included in Fig. 10 and shows good agreement with the air–water data but produces a progressively larger under-prediction as the viscosity increases. Thus, the commonly offered advice is not appropriate for highly viscous liquids.

7.2. Interfacial friction factors

Two-phase multiplier approaches are relatively dated. More modern analyses tend to produce predictive methods that are flow pattern dependent. Most of these data are believed to be in the annular flow regime where so-called film roughness models are prevalent. These methods model the interfacial shear stress through an interfacial friction factor, f_i, defined through

$$\tau_i = \frac{f_i}{2}\frac{u_G^2}{v_G} = \frac{f_i}{2}\left(\frac{x\dot{m}}{\alpha}\right)^2 v_G \tag{23}$$

The interfacial shear stress was obtained similarly to the wall shear stress, which was used in Eq. (23) to obtain the interfacial friction factor. The ranges of interfacial shear stress obtained are listed in Table 1. Again, as expected, the interfacial shear stress increases with increasing viscosity. However, an increasing discrepancy between the interfacial and wall shear stresses occurs as the viscosity increases.

Methods for predicting interfacial friction factors have been reported by Asali et al. (1985), Fukano and Furukawa (1998) and Ambrosini et al. (1991). The Ambrosini et al. (1991) method is a refinement to the Asali et al. (1985) method and therefore shows similar trends. The measured friction factor is compared to the Fukano and Furukawa (1998) and Ambrosini et al. (1991) methods in Fig. 11. The Fukano and Furukawa (1998) method represents the air–water data reasonably well. However, as the viscosity increases, the agreement becomes progressively worse with the prediction becoming progressively lower. This method was derived from data with viscosities of up to 10 mPa s but it clearly does not extrapolate to the viscosities used in this study. The predicted friction factors of Fukano and Furukawa (1998) are reasonably parallel with the measured values, offering some possibility of it forming the basis of a modified correlation. However, this is a film method and the film thickness element does not predict the void fraction for the 200 or 550 mPa s data (Fig. 8). The parallel behaviour disappeared when the Asali et al. (1985) method was used for the film thickness. The Ambrosini et al. (1991) method is sensitive to what is used for the entrained liquid fraction, especially at the higher qualities, shown as the lower friction factors in Fig. 11. Good agreement is shown between the method and the measurements from the air–water data. However, as the viscosity increases, over-prediction occurs. This film model is said to present a roughness effect to the core flow, the roughness being the surface waves on the liquid film. These waves are assumed proportional to the film thickness, causing the interfacial friction factor to depend on a non-dimensional film thickness, δ_G^+, defined by

$$\delta_G^+ = \frac{\delta}{\mu_G}\sqrt{\frac{\tau_i}{v_G}} \tag{24}$$

The data are suggesting that the roughness presented by highly viscous films is lower than those presented by the low viscosity equivalents, and that the roughness is not proportional to the film

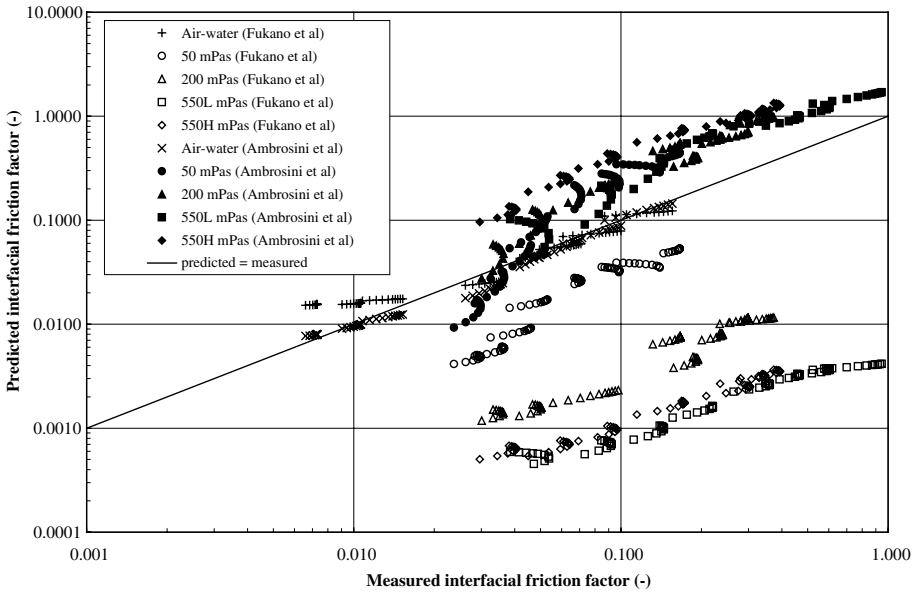

Fig. 11. Comparison of predicted and measured interfacial friction factor.

thickness. This is consistent with the change in the wave structure reported by Mori and Nakano (2001) and Kondo et al. (1999), where wave heights are shown to be lower, particularly if the roll wave regime has not been entered. The ranges of non-dimensional film thickness and film Reynolds numbers deduced from the test data are listed in Table 3.

The largest film to diameter ration is 0.1, justifying the use of Eq. (2). The non-dimensional film thickness is up to an order of magnitude larger than that obtained for low viscosity fluids. The values used by Asali et al. (1985) in forming their correlation were in the range 15–150.

Interfacial friction factors are shown as a variation with a Froud number function, FF, defined through

$$FF = \frac{1}{Fr^{1.28}} \left(\frac{v_G}{v_L} \right)^{0.912} \tag{25}$$

where the Froud number is defined by

Table 3
Interfacial friction factor parameters

Fluid viscosity (mPa s)	δ_G^+ range (–)	Film thickness (mm)	Film Reynolds number (–)
1	26–410	0.054–0.70	580–11300
50	30–1100	0.039–1.5	0.72–310
200	290–3000	0.27–2.5	2.5–80
550L	630–5500	0.43–2.7	1.6–35
550H	510–4600	0.38–2.2	1.5–30

$$Fr = \frac{u_G}{\sqrt{g\delta}} \tag{26}$$

in Fig. 12. A kind of smooth film–rough film behaviour is observed, with the smooth film data correlated by

$$f_i = 0.0983 FF^{0.249} \tag{27}$$

and the rough film data by

$$f_i = G \times FF \tag{28}$$

The bulk of the high viscosity data lie on the smooth line and the rough line with the constant 1.12. The data on this rough line can be identified as having a liquid Reynolds number of less than 40. All four of the viscous fluids are represented on these lines, indicating that a limiting behaviour may have been reached. Some of the 200 and 50 mPa s data points are not correlated by these lines. These data have constants of 0.614 and 0.347 respectively, constants that can be correlated by

$$G = 0.286 + 0.00153 \frac{\mu_L}{\mu_w} \tag{29}$$

where μ_w is the viscosity of water at 20 °C. This correlation gives 1.12 at 550 mPa s. A correlation scheme therefore emerges. If the liquid Reynolds number, found by assuming that the liquid flows alone in the pipe, is less than 40, the rough coefficient is 1.12; otherwise it comes from Eq. (29) provided it does not exceed 1.12. The transition Froud number function then follows by equating Eqs. (27) and (28). The friction factor is then found by assuming a smooth flow. If the resultant Froud number function is then less than the transition value, the smooth value is appropriate, otherwise the friction factor must be recalculated assuming a rough film. A comparison between

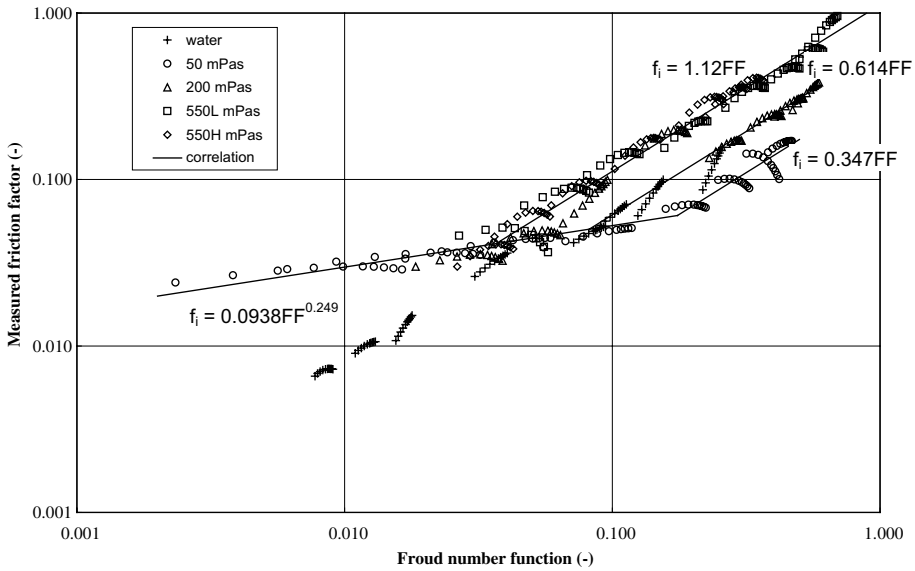

Fig. 12. Variation of measured friction factor with Froud number function.

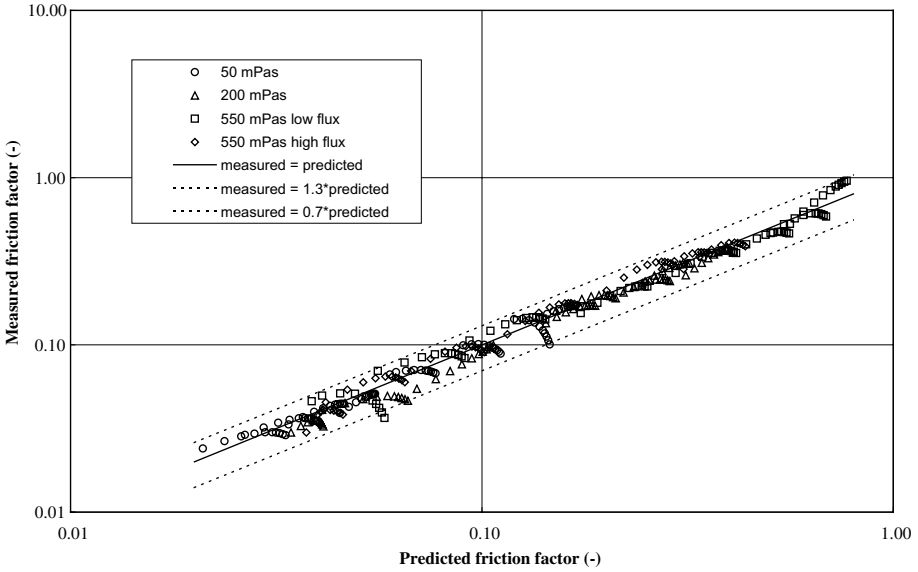

Fig. 13. Variation of measured friction factor with predicted friction factor.

the measured and predicted interfacial friction factor is given in Fig. 13. The root mean square error is 11%.

The air–water data are included in Fig. 12 for comparative purposes. Two observations are made. Firstly, the rough 50 mPa s data is moving towards a different trend to the other viscous data. Secondly, the water data follows a trend that is different from all of the other data. As is clear from Fig. 11, only the air–water data are well correlated by the non-dimensional gas thickness defined by Eq. (24). When deriving interfacial friction factors based on this approach, a minimum gas velocity of 25 m/s was imposed, Ambrosini et al. (1991) and Asali et al. (1985). This condition is reasonably met by all but the 550L mPa s datasets (Table 1). The cut-off point is imposed because, below it, gravity is said to affect the film–core interface, an effect that could be affected by the thickness of the liquid film, a quantity much larger with highly viscous liquids. Fig. 12 may be depicting a complex transition from the fully rough behaviour ($G = 1.12$) to the low viscosity behaviour characterised by the Ambrosini et al. (1991) approach. There are insufficient data do establish the full nature of this transition. However, a non-dimensional number that separated gravity from the low viscosity data may allow other effects due to high viscosity to be more easily defined. The transition that occurs between the low and high viscosity fluid probably results from a change in the interfacial behaviour observed by Mori and Nakano (2001) and Kondo et al. (1999).

8. Sonic flows

The sonic mass fluxes were calculated using an annular flow model based on similar assumptions to those outlined for the subsonic flows in Section 4. The momentum equation was therefore

again given by Eq. (3). Isothermal flow assumption, Eq. (6), is inappropriate for a sonic flow and was replaced by the energy equation

$$\frac{x}{(x+\varepsilon(1-x))}\left(\frac{\gamma p}{(\gamma-1)}\frac{\mathrm{d}v_{\mathrm{G}}}{\mathrm{d}z}+\frac{v_{\mathrm{G}}}{(\gamma-1)}\frac{\mathrm{d}p}{\mathrm{d}z}\right)=\frac{4\tau_{\mathrm{i}}v_{\mathrm{c}}}{(D-2\delta)}-\frac{\mathrm{d}w}{\mathrm{d}z} \tag{30}$$

where γ is the isentropic index for air and $\mathrm{d}w/\mathrm{d}z$ is the work done on the liquid film by the core flow, which was estimated from

$$\frac{\mathrm{d}w}{\mathrm{d}z}=\frac{4\tau_{\mathrm{i}}v_{\mathrm{c}}}{(D-2\delta)}\frac{u_{LF}}{u_{\mathrm{G}}} \tag{31}$$

and made little contribution to the predictions made at the test conditions. This energy equation is based on the same assumptions as the momentum equation, but additionally assumes that the entrained liquid flow is isothermal and the core flow is adiabatic. The film thickness was calculated as before. The interfacial and wall shear stresses were assumed to be equal, eliminating the need of Eq. (2). This latter assumption was approximately true even for the subsonic tests (Table 1). The shear stress was calculated using two approaches, the Chisholm C approach and the interfacial friction factor approach. The Chisholm C method used Eqs. (20) and (21) with a coefficient of 25. The interfacial friction factor approach used the Ambrosini et al. (1991) method for air–water flows and Eqs. (25)–(29) for the 50 mPa s flows. The sonic mass flux was taken to occur when $\mathrm{d}z/\mathrm{d}p$ was zero at the pipe exit. The entrained liquid fraction was estimated at the beginning of each integration step. For the air–water flows it was obtained from the method of Govan et al. (1988) by assuming a balance between the rates of entrained and deposited droplets. The values for the air–glycerine flows were obtained from the relationships given in Section 6. A comparison between the calculated and measured sonic mass fluxes is given in Fig. 14. The Chisholm C ap-

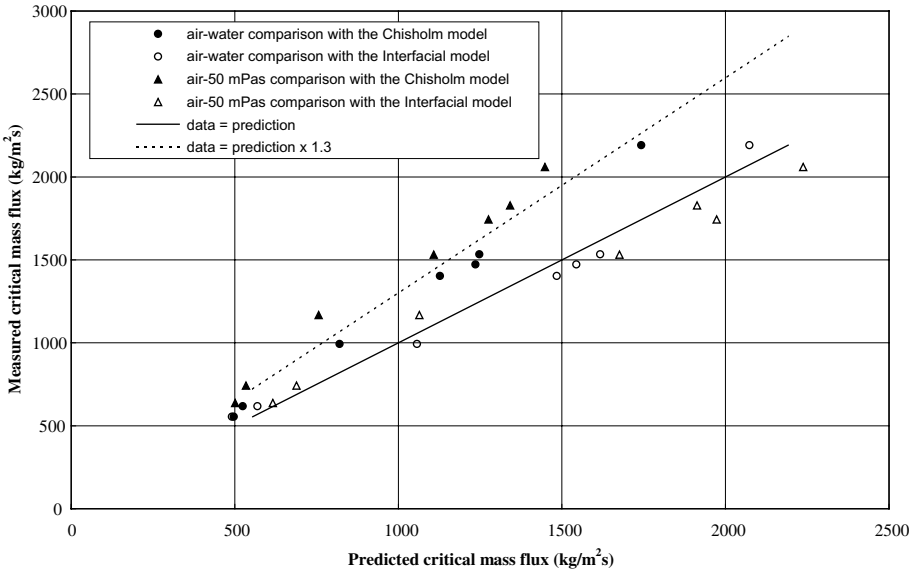

Fig. 14. Comparison of measured and predicted critical mass flux.

proach under-predicts the critical mass flux by about 30%, whereas the interfacial friction factor model gets it about right. Typical pressure distribution comparisons between data and measurements are given for an order of magnitude change in quality in Figs. 15 and 16. The air–water predictions offer a better agreement than the air–glycerine predictions, as might have been

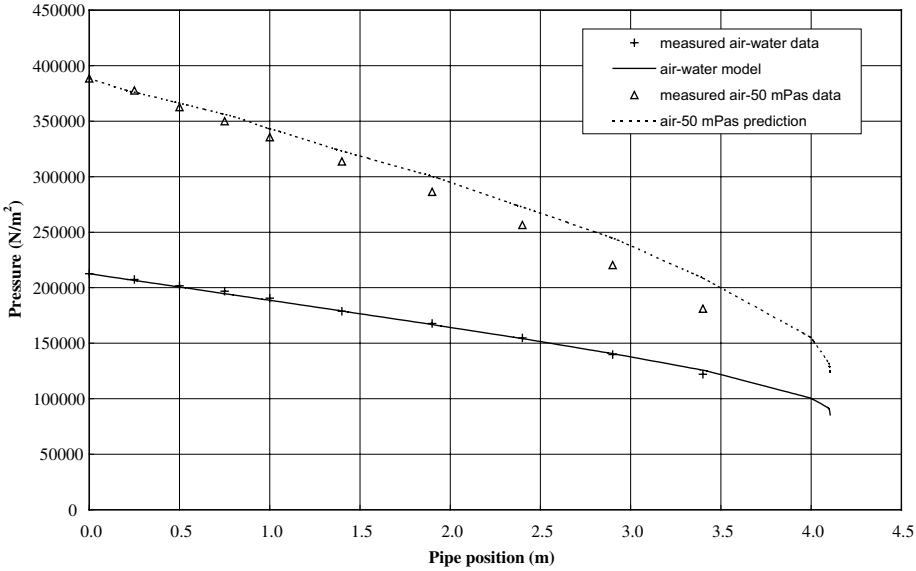

Fig. 15. Comparison of measured and predicted pressure at a quality of 0.06.

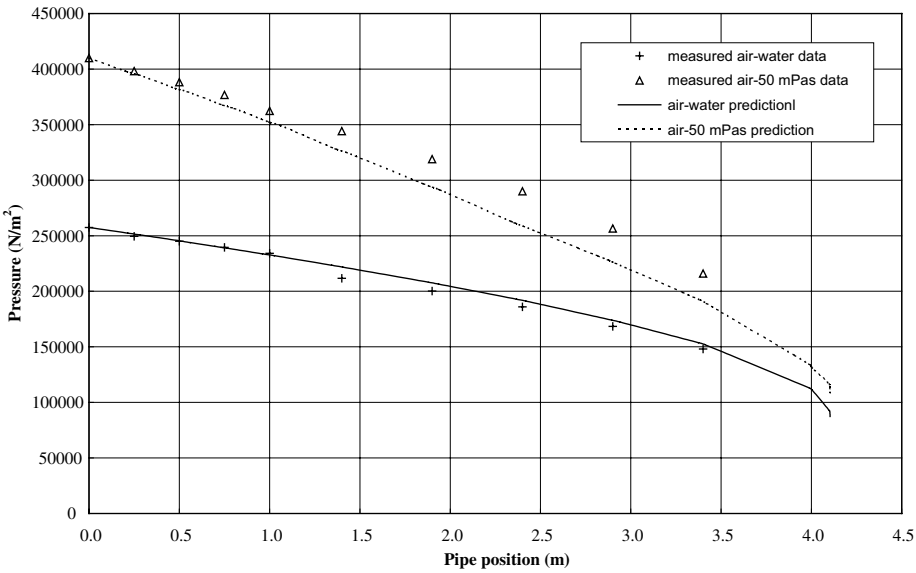

Fig. 16. Comparison of measured and predicted pressure at a quality of 0.6.

expected given the uncertainty in the entrained liquid fractions used with the 50 mPa s data. Never the less, the interfacial model is clearly the only one that extends across the Mach number range, offering friction estimation independent of Mach number, as occurs in single-phase flows.

9. Discussion and conclusion

Two-phase flows with a highly viscous liquid phase are not well understood. In extending current knowledge two approaches are possible, a flow pattern independent or a flow pattern dependent approach.

Approaches independent of flow pattern require correlations for void fraction, momentum flux and frictional pressure gradient. This study has shown that existing momentum flux and void fraction methods do not extend to the highly viscous range, Figs. 5 and 7, and that only the Chisholm C model has any success in representing the frictional pressure gradient (Fig. 9). However, its C coefficient is different from that associated with low viscosity fluids and it does not extend across the full Mach number range (Fig. 14). This latter problem is also true in low viscosity applications, Chisholm (1983).

Developing flow pattern dependent methods has different difficulties. The existing flow pattern maps do not apply, making the application of these models problematic. For annular flows, the criterion for the onset of entrained liquid fraction and the models for predicting its level are invalid. This study has shown that for the annular flow regime, Asali et al.'s method (1985) can be used to determine the liquid film thickness, Fig. 7, and the interfacial friction factor can be found from the proposed correlation. This approach also extends across the Mach number range (Figs. 14–16). However, further work needs to be undertaken to allow the determination of the entrained liquid fraction, and to understand the transition from the low viscosity to the high viscosity behaviour evident in the interfacial friction factor analysis (Fig. 12). Developing a flow pattern dependent method is therefore the preferred way forward as this offers the most benefits. This will require this work to be extended and for viscous effects on other flow patterns to be investigated.

Acknowledgements

The authors gratefully acknowledge the financial support given to this work by the European Commission (DGXII—Science, Research and Development) through the INOVVATOR project (Environment and Climate programme).

References

Alvi, S.H., Sridharan, K., Lakshmana Rao, N.S., 1978. Loss characteristics of orifices and nozzles. J. Fluid Eng. 100, 299–307.

Ambrosini, W., Andreussi, P., Azzopardi, B.J., 1991. A physically based correlation for drop size in annular flow. Int. J. Multiphase Flow 17, 497–507.

Asali, J.C., Hanratty, T.J., Andreussi, P., 1985. Interfacial drag and film height for vertical annular flow. AIChE J. 31, 895–902.

Baker, O., 1954. Simultaneous flow of oil and gas. Oil Gas J. 53, 185–190.
Campanile, F., Azzopardi, B.J., 2001. Two-phase downflow and atomisation of very viscous liquids. In: 4th International Conference on Multiphase Flow, New Orleans, 27th May–1st June, Paper 827.
Chisholm, D., 1962. The influence of viscosity and liquid flow rate on the phase velocities during two-phase flow. NEL Report No. 33, National Engineering Laboratory, East Kilbride, Glasgow.
Chisholm, D., 1973. Pressure gradients due to friction during the flow of evaporating two-phase mixtures in smooth tubes and channels. Int. J. Heat Mass Transfer 16, 347–358.
Chisholm, D., 1983. Two-phase Flow in Pipelines and Heat Exchangers. George Goodwin, London and New York.
Chisholm, D., Laird, A.D.K., 1958. Two-phase flow in rough tubes. Trans. ASME 80, 276–286.
Chong, L.Y., Azzopardi, B.J., Hankins, N.P., 2001, Entrainment rate in annular two-phase flow. Paper 27, 6th UK Heat Transfer Conference, Nottingham, September 10–11.
Collier, J.G., Thome, J.R., 1994. Convective Boiling and Condensation, third ed. Clarendon press, Oxford.
Friedel, L., 1979. Improved friction pressure drop correlation for horizontal and vertical two-phase pipe flow. Presented at the European Two-Phase Flow Group Meeting, Ispra, Italy, Paper E2.
Fukano, T., Furukawa, T., 1998. Prediction of the effects of liquid viscosity on interfacial shear stress and frictional pressure drop in vertical upward gas–liquid annular flow. Int. J. Multiphase flow 24, 587–603.
Furukawa, T., Fukano, T., 2001. Effects of liquid viscosity on flow patterns in vertical upward gas-liquid two-phase flow. Int. J. Multiphase flow 27, 1109–1126.
Govan, A.H., Hewitt, G.F., Bott, T.R., Owen, D.G., 1988. An improved CHF modelling Code. In: 2nd UK National Conference on Heat-Transfer. University of Strathclyde, Glasgow, Paper C175/88, pp. 33–48.
Hewit, G.F., Roberts, D.N., 1969. Studies of two-phase flow patterns in simultaneous flash and X-ray photography. AERE-M2159, Harwell.
Holt, A.J., Azzopardi, B.J, Biddulph, M.W., 1999. Calculation of two-phase pressure drop for vertical upflow in narrow passages by means of a flow pattern specific model. Trans. I. Chem. E Part A 77, 7–15.
Ishii, M., Grolmes, M.A., 1975. Inception criteria for droplet entrainment in two-phase concurrent film flow. AIChE J. 21, 308–318.
Kondo, Y., Mori, K., Yagishita, T., Nakabo, A., 1999. Effect of liquid viscosity on wave behaviour in gas–liquid two-phase flow. In: Proc. 5th ASME/JSME Joint thermal conference, San Diego, California, March 15–19. pp. 1–8.
McNeil, D.A., 1998. Two-phase momentum flux in pipes and its application to incompressible flow in nozzles. Proc. Inst. Mech. Engrs.: Part C 212, 631–641.
Mori, K., Nakano, K., 2001. Effects of liquid viscosity on inception of disturbance waves and droplets in gas–liquid two phase flow. Experimental Heat Transfer, Fluid Mechanics and Thermodynamics, Thessaloniki, 1829–1834.
Pan, L., Hanratty, T.J., 2002. Correlation of entrainment for annular flow in vertical pipes. Int. J. Multiphase Flow 28, 363–384.
Premoli, A., Francesco, D., Prima, A., 1970. An empirical correlation for evaluating two-phase mixture density under adiabatic conditions. European Two-Phase Flow Group Meeting, Milan.
Richter, H.J., 1983. Separated two-phase flow model: applications to critical two-phase flow. Int. J. Multiphase Flow 9, 511–530.